Size-independent phase distinction in dispersed two-phase flows

David de Souza, Till Zürner, Romain Monchaux

Noname manuscript No.
(will be inserted by the editor)

Size-independent phase distinction in dispersed two-phase flows

David De Souza · Till Zürner · Romain Monchaux

Received: date / Accepted: date

Abstract Dispersed two phase flows cover a wide range of natural phenomenon and technological applications. When studying such complex systems, having access to the velocities of both phases is necessary to fully understand their dynamics. While data from both phases can be obtained in numerical simulations, this can prove more difficult to perform with experimental measurements. In this article, a new method to separate inertial particles from tracers in a two-dimensional laser sheet is described. By using a two camera acquisition system combined with an optical filter, the two phases can successfully be segregated, without relying on an apparent size or intensity difference between inertial particles and tracers. This allows for the velocities and positions of the particles to be measured in conjunction with the velocity field of the carrying phase. A series of tests are performed on the method. In addition to ensuring that the method functions in a satisfactory manner, these tests give guidelines on how to use the method correctly. To illustrate an application of this method, measurement results of ceramic particles settling in still water are presented.

Keywords Particle laden flow · PIV · PTV · Dyed tracers · Optical filtering

This work was supported by the French Direction Générale de l'Armement (DGA) through the Agence de l'Innovation de Défense (AID).

D. De Souza · T. Zürner · R. Monchaux
Institut des Sciences de la Mécanique et Applications Industrielles (IMSIA),
ENSTA-Paris / CNRS / CEA / EDF / Institut Polytechnique de Paris,
828 Boulevard des Maréchaux, 91120 Palaiseau, France
E-mail: romain.monchaux@ensta-paris.fr

1 Introduction

Particle laden flows are ubiquitous in natural and industrial systems, and have received much attention in the last decades. When particle inertia is different from that of the fluid, the particle dynamic deviate from that of tracers which exactly follow fluid elements, and are usually used in fluid metrology to gain access to the fluid velocity field. Inertial particle trajectories sample the flow non-uniformly (Maxey and Corrsin, 1980) leading to preferential concentration, some regions of the flow being more visited than others due to their local properties (high/low strain or vorticity, vanishing acceleration...). When the particle loading is high enough, preferential concentration can lead to the formation of denser regions where particles accumulate as originally found by Brown and Roshko (1974). This so called clustering can also be a consequence of the path history of particles and can thus occur in any region of the flow, regardless of its local properties (Gustavsson and Mehlig, 2011). The high intermittency in the concentration field due to clustering and/or preferential concentration can be an issue in many applications (e.g. for pollutant, plankton dispersion, mixing or fuel combustion in engines), but it may also have dramatic impacts on other relevant issues of particle laden flows: collisions, settling velocity alteration and carrier phase modulation. The collision probability depends on both the local particle concentration field and on the local velocity gradients (Falkovich et al., 2002). The settling velocity is altered as soon as the carrier flow is turbulent (Maxey and Corrsin, 1980) but also when the local particle concentration is dense enough (Aliseda et al., 2002; Monchaux and Dejoan, 2017; Huck et al., 2018). Both cases depend non-trivially on many physical parameters (e.g. volume loading, phase density ra-

tios, turbulence level or particle size). How the back reaction by the particles on the continuous phase modifies the carrier flow is just as complex and sensitive to the same parameters (Elghobashi and Truesdell, 1993; Eaton, 2009).

As direct on-site measurements of these processes (e.g. in clouds, marine snow, ash clouds or combustion chambers) are rarely possible, model experiments and numerical simulations are traditionally used to investigate the very rich physics of these flows. Due to the complexity of solving the flow in the vicinity of large numbers of finite sized particles, this kind of direct approach is still limited (Homann and Bec, 2010; Lucci et al., 2010). Usually, the Navier-Stokes equations are solved for the fluid and model equations are used for the particles. Unfortunately, the available analytical model equations for the dynamics of inertial particles are obtained under the limiting assumptions of point particles and very large density ratio (Maxey and Riley, 1983; Gatignol, 1983) and involve many terms that are most of the time neglected in numerical studies. In addition, to reduce the computation time required to explore the wide parameter space described above, most numerical studies do not consider the back reaction particles exert on the fluid. Providing empirical models that allow for this back reaction to be numerically implemented without solving the whole velocity field in the neighbourhood of each particle is thus an essential challenge for the coming years.

To address this challenge, as well as providing model free data to understand the complex and intricate roles of the large number of parameters controlling particle laden flows, experiments have to provide detailed measurements in both phases, at the same time and location. Such measurements provide us with the slip velocity between the two phases, fluid-particle correlations or at least fluid statistics at the particle positions. All these quantities are key ingredients to understand the mechanisms at work in preferential concentration, clustering, settling velocity and collision alteration, and carrier phase modulation. Even though the development of such simultaneous measurements in both phases has started two decades ago (Towers et al., 1999), it is still far from being routinely used in laboratories and no commercial solution is available yet.

Fluid flow measurements are now available in any number of dimensions. Three dimensional (3D) Eulerian velocity fields are accessible through particle image velocimetry (PIV), that can even be time-resolved under certain conditions. Using particle tracking velocimetry (PTV), Lagrangian particle trajectories can also be measured at sufficiently high time resolutions to allow acceleration statistics to be computed (Ouellette et al., 2008). The main drawback of the 3D measurements is its usually very limited volume. Probing wider regions of flows from both PIV and PTV is still the private preserve of two dimensional (2D) systems. Pointwise (0D) systems are also often employed in multiphase flow studies, particularly in wind tunnels to collect one dimensional (1D) data sets under Taylor hypothesis assumptions. These systems can be intrusive (hot wires, optical probes) or not (laser Doppler anemometer, phase Doppler particle analysis), some of them being able to discriminate between phases, see for example Muste et al. (1998). However, it has been recently shown that the acquired 1D data may suffer from very strong biases that are difficult to overcome (Mora et al., 2018). In the following we will focus on 2D systems.

Most 2D systems can be equally used to perform measurements on fluid tracers or on inertial particles. Indeed, as they are usually designed to see and/or follow tracers that are smaller than inertial particles, it is thus quite simple to use these same systems to image and/or track inertial particles that are often more visible on the acquired images than the tracers. The difficulty in measuring both phases thus mainly relies on the simultaneity, as these systems are usually not made to perform PIV on the fluid and PTV on the inertial particles at the same time. Several groups have designed such coupled measurement systems (see next two paragraphs) but, as mentioned above, it still remains a challenging issue. As both independent measurements are well developed, the key issue for simultaneously probing both phase is to manage the segregation between tracers and inertial particles. Depending on the carrier fluid, usually air or water, the tracer characteristics can be quite different. In water they are typically almost neutrally buoyant spherical particles whose diameters can range between 5 to 30 µm. In air, 1 to 2 µm oil droplets are traditionally used, but are increasingly replaced by 300 µm inflated neutrally buoyant soap bubbles. Regarding inertial particles, the range of particle size used by the different authors varies on orders of magnitude according to the wide range of corresponding applications. Larger particles are usually sand or beads whose diameters can be as large as a few millimetres while the smallest can be even smaller than tracers. While PIV tracers are designed to diffuse as much light as possible, inertial particles in general cannot be tailored to this purpose and come as they are. Depending on their size and material, they may scatter very little light.

Most successes in simultaneous fluid/particle measurements have been obtained when a large scale separation exists between particles and tracers. In this case, a classical 2D PIV/PTV system is sufficient and parti-

cles and tracers are acquired on the same image by a single camera. Multiple authors designed different post-processing algorithms to achieve the segregation: simple discrimination by spot size has been used since the early two phase measurements by Chen and Fan (1992) or Hassan et al. (1992), but more sophisticated algorithms taking into account, for example, the relative brightness of tracers and particles (Khalitov and Longmire, 2002; Petersen et al., 2019), or filtering the tracers as a high frequency noise (Kiger and Pan, 2000) have been proposed. In many cases, the material and size differences between tracers and particles are obviously used in the separation algorithms.

In the absence of scale separation, a relevant idea is to use fluorescent dye. Under laser illumination, dyed tracers will emit light at a shifted wavelength while particles will only diffuse the incoming light as is. This seems to provide an easy way to perform the segregation. Single camera acquisitions can still be relevant if a colour camera is used. With green 532 nm laser and rhodamin coated tracers (a classical set-up), the green channel will ideally only see the particles while the red channel would only see the tracers. See Towers et al. (1999) for a more sophisticated application where both phases are dyed differently and a triple pulse laser is used to discriminate them. Unfortunately, the low resolution of colour cameras, the interpolation schemes used to compensate for the colour filtered array of pixels and the high level of induced pixel locking incite to avoid colour cameras. The obvious alternative is to use two cameras equipped with colour filters and aiming at the same field of view. The main issue then becomes the difficulty in matching the acquired fields of view. This can be achieved by using beam splitters, or by positioning both cameras very close to each other, aiming at almost the same field of view, and using a stereoscopic PIV calibration procedure to match the fields of view (the latter being our proposition). The use of a beam splitter avoids sophisticated calibration procedures since both cameras actually aim at the same field of view, but it implies a somewhat complex mounting and more importantly the loss of half the light budget, which may be an issue when particles do not diffuse much light. This was nonetheless successfully implemented by Elhimer et al. (2017). In their study, a "cross-talk" between the two cameras remained. In fact, the inertial particles used were much larger than the tracers (more than 1 mm in diameter) and, due to their size, faint images of the inertial particles could be seen on the tracer images, as the fluorescent light emitted by the tracers was also scattered by the particles. This was solved with an additional post processing to separate particles from tracers thanks to their difference in intensity. The unusual use of a stereoscopic PIV system is made more appropriate and accurate nowadays with the recent development of so-called self-calibration algorithms that allow to almost perfectly match both fields of views. For more details on this calibration procedure see Wieneke (2005). In any case (colour or greyscale cameras, beam splitters or not), experimentalists are left with two sets of images. On the "red" one, only dyed tracers are visible, the flow field is thus easily accessible. However, on the "green" one, it might be more complicated. Indeed, the efficiency of the absorption and emission of the incoming wavelength by the dyed tracers is not 100%. As a result, tracers also directly scatter a portion of the laser light and are thus visible on the "green" images alongside the particles. Poelma et al. (2007) also refer to this as "cross-talk" between images. In their study, they manage to get rid of this cross-talk because, due to scale and brightness separation, the tracers' grey level is within background noise on the "green" images. When particles and tracers have similar sizes and when the particle material does not scatter much light, a way to remove tracers from these images has to be found.

In this article, we propose a method to achieve simultaneous velocity measurements of particles and tracers when no scale or brightness separation is present, by masking the tracers on images with inertial particles. The method developed here is generic and can be applied with most standard stereoscopic PIV systems. Section 2 of this article describes this method and outlines its potential pitfalls. To ensure that the method works and to examine its limitations, various tests are performed on experimental data sets. These testing procedures and their results are presented in section 3. Finally, section 4 gives recommendations on the method application and showcases some results from real-life experiments before concluding in section 5.

2 Tracer masking method

2.1 Method description

An overview of the method can be found in figure 1. The method starts from two synchronised image sources: one camera recording both particles and tracers, and one camera that only sees tracers. In the following these are denoted as particle camera and tracer camera, respectively. Both cameras record greyscale images, giving the light intensities $I_\mathrm{P}(x, y)$ for the particle camera and $I_\mathrm{T}(x, y)$ for the tracer camera.

The fluid velocity field can be calculated directly from I_T using PIV. To perform PTV on I_P, inertial particles have to be distinguished from tracers. This is

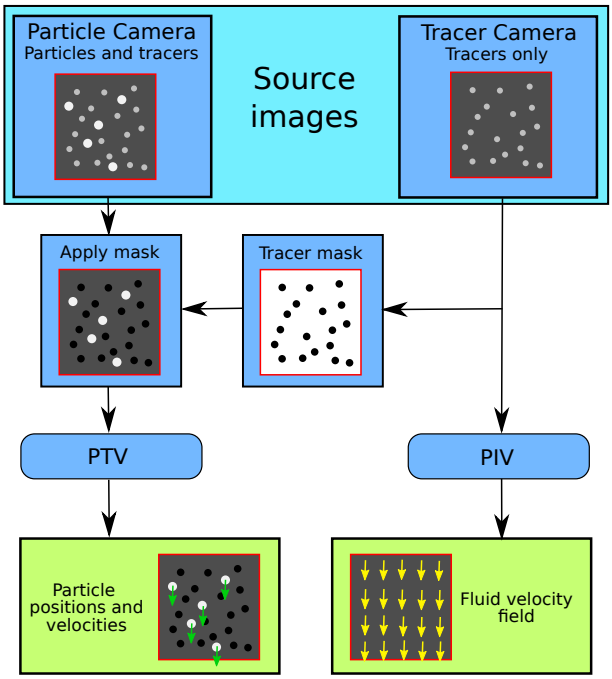

Fig. 1: Flowchart of the method for simultaneous particle tracking and fluid velocity measurements by tracer masking. The illustration frames display particle and tracers with exaggerated color and size difference for easier distinction only.

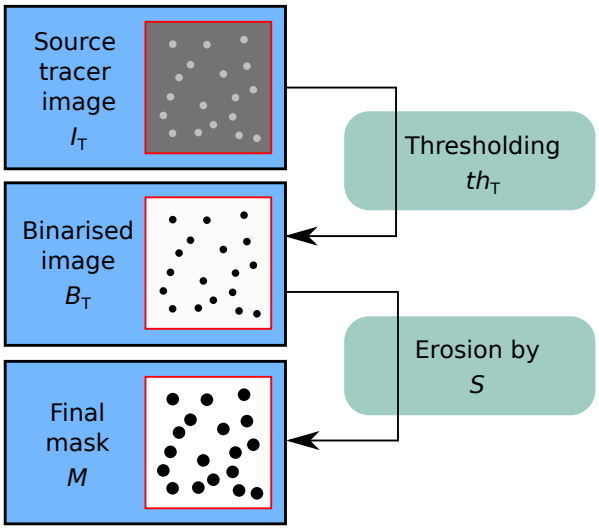

Fig. 2: Flowchart of the mask creation process. On B_T and M, areas in white represent pixel values of one and areas in black are pixel values of zero.

achieved by creating a tracer mask from I_T that effectively removes the tracers from I_P. The inertial particles can then be tracked on the resulting filtered images. The characteristics on how to perform a good PIV or PTV will not be discussed in this article, and the parameters involved in these techniques will only be mentioned when relevant to the topic.

A flowchart of the mask creation process can be found in figure 2. The goal is to set the intensities of all pixels belonging to a tracer in I_P to zero. The first step is to detect the tracers on I_T. This is done by turning I_T into a binary image B_T that sets all pixels that belongs to a tracer in I_T with zero:

$$B_T(x,y) = \begin{cases} 1, & I_T(x,y) < th_T \\ 0, & I_T(x,y) \geq th_T \end{cases}, \quad (1)$$

where th_T is the intensity threshold defining whether a pixel belongs to a tracer or not. Using the colour code of figure 2, the area of interest here becomes a white background, while the black spots of the tracers are the regions that will be discarded. However, depending on the configuration of the image sources, small discrepancies in shape, intensity, or even positions of the tracers might exist between I_P and I_T. These are further discussed in section 2.2. To accommodate for these discrepancies, the second step of the mask creation process increases the area of the tracers in B_T. This is done by performing an erosion of the white background around the black tracer spots using a structuring element S. This erosion is a morphological operation that will widen every area of B_T where pixels are at zero, i.e., marked as a tracer position. Examples of structuring elements can be found in figure 3. The larger S is, the more the black area will widen. For example, S_1 does not change B_T, S_5 sets to zero all pixels vertically or horizontally adjacent to a zero, S_9 adds all pixels diagonally adjacent, etc. More details on such morphological operations can be found in Haralick et al. (1987). The result of the erosion of B_T by S is the final tracer mask M.

The tracers are then removed from I_P. This removal is done by applying M to I_P with a simple pixel-wise multiplication:

$$I_M(x,y) = I_P(x,y)M(x,y), \quad (2)$$

where I_M is the final particle image, without tracers. The positions and velocities of the inertial particles can finally be obtained by performing PTV on I_M.

2.2 Error assessment

Generally speaking, errors resulting from the application of this method can have two main origins. The

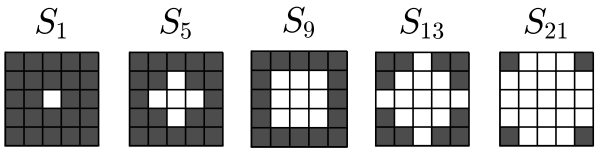

Fig. 3: Examples of structural elements, which are usually small binary sets. Each sub-square represents a pixel, zeros are in black, ones are in white. For the purpose of this article, they are designated by the number of pixels having a value of one. Essentially, for an erosion, any pixel that is at zero will result in all neighbouring pixels to be turned to zero to match the shape of S. For a given reference pixel at zero: S_1 does not change the image, S_5 turns all pixels vertically and horizontally adjacent to the reference pixel to zero, S_9 does the same but also sets pixels diagonally adjacent to zero, and so on. The structural elements represented here are also the ones used in the testing procedures of section 3.

discrepancies in the tracers properties between the two source images I_P and I_T constitute one of these origins. For example, if a system with two cameras is used, a tracer can be projected onto each camera with different intensities, shapes and positions. A difference in intensity is not an issue for the method presented here, as the choice of th_T is informed by the intensities of tracers in I_T only, and tracers masked in I_T will be removed from I_P regardless of their intensities. However, differences in shape or position may lead to M not properly covering the tracers in I_P. In this instance, tracers detected in I_T may remain in I_M and particles might have been erroneously deleted by the mask. The second category of error sources is an inadequate choice of the method parameters th_T and S. Going to extreme cases, if th_T is low enough to catch the background noise level of I_T, pixels that are not from tracers will be set to zero in B_T, resulting in an unnecessary loss of data in I_M. Conversely, putting th_T too high will leave all tracers in the image. For S, if it is too small, the erosion will not make up for the discrepancies between I_P and I_T. But picking one that is too big will end up with a mask that deletes portions of the image that could have been kept.

From these two origins, three main errors can occur: tracers can remain in I_M, particles can be completely removed when applying the mask or they can be partially removed. These errors will be referred to as false particle error, erased particle error and altered particle error respectively. First, the false particle error adds false positives, which can skew the tracking results as tracers are mistaken as particles. Second, the erased particle error leads to false negatives, resulting in a loss of data. Finally, the altered particle error will change the particle's detected position, as altering the shape of a particle will change where the center of the particle is detected. In addition to their effects on the trajectories computed by PTV, these errors will influence the apparent concentration field, which is crucial to understanding the mechanics of dispersed two-phase flow systems.

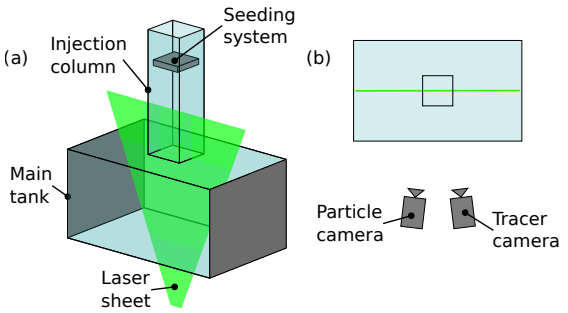

Fig. 4: Experimental set-up: (a) overview without the cameras, (b) top view.

3 Method Validation

To evaluate the response of the method to the errors outlined in section 2.2, two testing procedures have been devised. These procedures involve images from experiments as the basis of the tests. This section first describes the experimental set-up used to obtain these images before covering each testing procedure and their results.

3.1 Experimental set-up

An illustration of the experimental set-up can be found in figure 4. The main part is a tank of dimension $350 \times 480 \times 350$ mm^3. A column, of square cross-section with side length 130 mm and height 410 mm, sits on top of it. This structure is filled with water. On top of the column, a vibrating sieve serves as the seeding system for the apparatus. Particle injection is controlled by pouring particles onto the sieve and turning the vibration on.

Observations are done in the main tank. Images are recorded with a LaVision stereo PIV acquisition system of two VC-Imager SX 4M cameras synchronised with a vertical pulsed laser sheet of wavelength 532 nm produced by an Nd:YAG Dual Power 135-15 laser from

Dantec Dynamics. The tracers used are coated in rhodamine. Accordingly, the tracer camera is equipped with an optical filter that lets the fluoresced light emitted by the rhodamine of wavelength above 570 nm pass through and blocks the laser wavelength. Both cameras are calibrated on the same area of the laser sheet using a dotted plate and the self-calibration method previously mentioned.

The two cameras record two images or frames each, in quick succession, and the time in between the two frames can range from 10 to 30000 µs. These double frames from both cameras are recorded with an acquisition frequency of up to 15 Hz. After applying the tracer removal method, the instantaneous particle positions and velocities, and the fluid velocity field are obtained. However, the maximal sampling frequency of the system does not allow to track particles between double frames, i.e., long-term particle trajectories are not accessible in the present experiments. In other terms, PTV is performed on each double frame recorded as if it were independent of the previous and following double frames in the experiment. However, the method presented in this article does not depend on the acquisition frequency and and can be applied to systems with higher sampling rates.

The images have a resolution of 1700 by 2375 pixels, with each pixel having an intensity ranging from 0 to 4095. Overall the acquisition system has a scaling factor of 13.7 pixel/mm which then corresponds to an area of 124 by 173 mm of the laser sheet used for observation. For each experiment, an image of the minimal intensities observed on the experimental run is computed and then subtracted from all images to increase the signal to noise ratio. After this operation, the images typically have a background noise below 10 in pixel intensity. The apparent diameter in pixels of the particles obviously depend on their size and the material they are made of but the smallest tested up to now span 4 to 5 pixels. The rhodamine coated tracers have an apparent diameter of 2 to 3 pixels.

3.2 Tracer removal test procedure

The first testing procedure is a tracer elimination check done mainly to test the method's response to the errors from the discrepancies between I_P and I_T, and how its parameters can be tuned to yield reliable results. A flowchart of this procedure can be found in figure 5. It is designed to ensure that the method removes all tracers while deleting as little of the image as possible. The test images I_P and I_T used here contain only tracers. That way when applying the tracer masking method, the resulting I_M should ideally be empty.

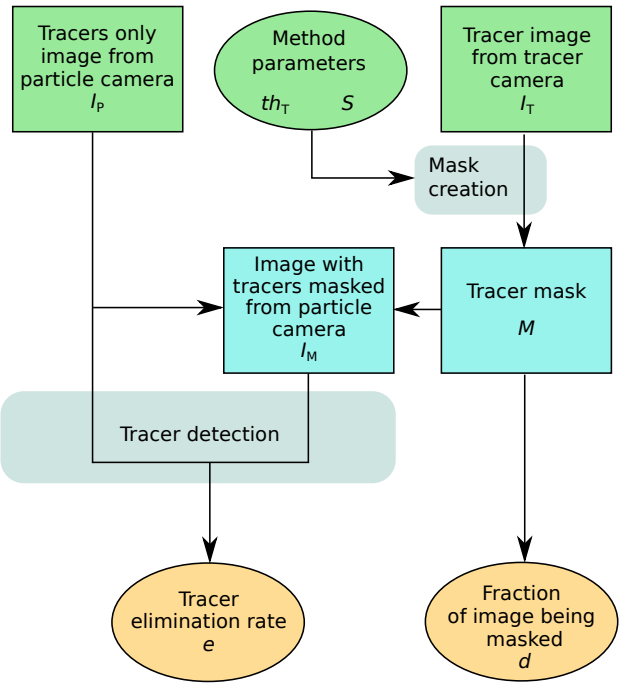

Fig. 5: Flowchart of the testing procedure on errors coming from discrepancies between I_P and I_T.

Then, by applying PTV on I_M, any particle detected will in fact be a tracer that was not removed. The images I_P and I_T used were taken from experiments conducted on the device described in section 3.1. For a given pair of tracer-only images I_P and I_T, the only other inputs for the testing procedure are th_T and S, the parameters of the tracer removal method. A particle detection (i.e., the first step of PTV) is performed on the tracer-only particle image I_P and on the masked image I_M, resulting in a number of detected particles for each of these images. These numbers will respectively be called N_P and N_M. A tracer elimination rate e is then computed as $e = (N_\mathrm{P} - N_\mathrm{M})/N_\mathrm{P}$. In addition, the fraction d of the image deleted by the method can also be computed from the mask itself, as the number of pixels at zero in the mask over the total number of pixels. An overview of the inputs used for this testing procedure can be found in table 1.

Both e and d take values between zero and one. Ideally, e should be as close to one as possible and d should remain close to zero. In figure 6, e is plotted against d, separated and coloured by values of th_T used in the tests. th_T is shown to have a clear impact on both e and d. The observed response can be explained as follows. Taking a value for th_T that is too low will identify the background noise of the image as tracers and extend the

Table 1: Overview of the parameters tested in the tracer removal test procedure (section 3.2), and of the characteristics of the images tested. For an illustration of the structuring elements' shapes, see figure 3. All the images used are from different experimental runs. The tracer brightness given is for well lit tracers in the laser sheet, i.e. tracers that are fully in the laser sheet.

Parameter	**Values, range or number**	**Unit**
th_T	{5; 10; 20; 35; 50; 70}	greyscale intensity
Structuring elements' shapes	S_1, S_5, S_9, S_{13}, S_{21}	-
Number of images	77	-
Tracer diameter	2 to 3	pixel

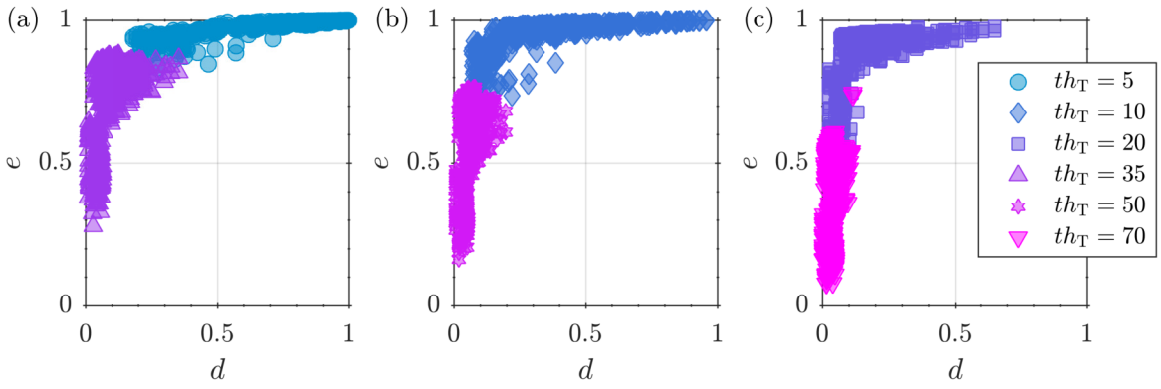

Fig. 6: Scatter plots of e against d, distinguished by values of th_T, for all S. These are spread in three separate plots for clarity, to avoid overlapping too many points. Among the tested thresholds, $th_\mathrm{T} = 20$ (squares) results most consistently in low d and high e.

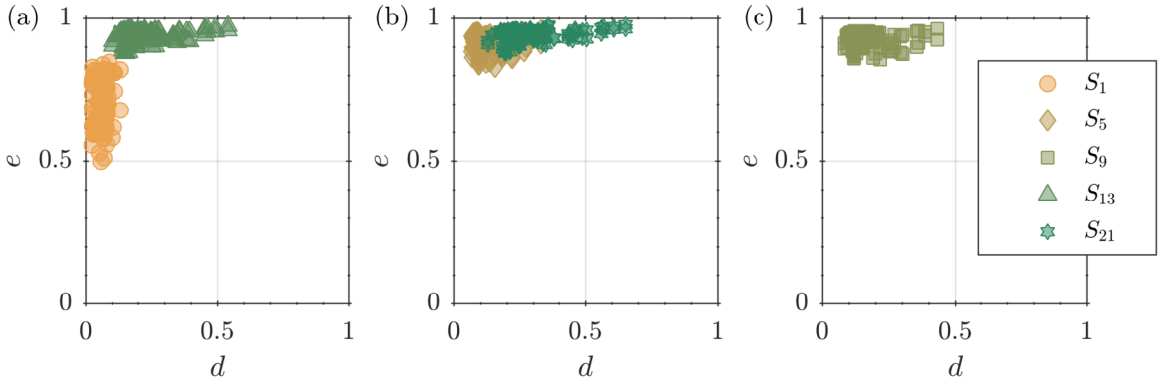

Fig. 7: Scatter plots of e against d, for $th_\mathrm{T} = 20$ (square markers in figure 6(c)), distinguished by S. These are spread in three separate plots for clarity, to avoid overlapping too many points. S_5 and S_9 lead to the best results on terms of e and d.

area removed by the mask to regions where there are in fact no tracers. This results in all tracers being removed but at the cost of deleting a large portion of the image, thus in high e and high d. On the other hand, setting a value for th_{T} that is too high will miss a lot of the tracers in I_{T}, causing them to remain after M has been applied, as described in section 2.2. As fewer tracers are marked for removal, a smaller fraction of the image will be deleted, which leads to both low e and low d. th_{T} needs to be selected carefully in order to get appropriate results, i.e., high e and low d. In the tests presented here, $th_{\mathrm{T}} = 20$ (squares in figure 6) seems to achieves the best results in terms of high tracer elimination e and low image deletion d. Note that this value is specific to the images tested here, and depends on the image acquisition system and potential post-processing applied to the image (such as background image subtraction or noise filtering). The method may still perform well for $th_{\mathrm{T}} < 20$, as, even if more of the image is deleted, more tracers will be removed without necessarily diminishing the number of inertial particles that can still be found by the method.

The impact of S can then be seen in figure 7, where e is plotted against d for a fixed $th_{\mathrm{T}} = 20$, separated and coloured by S. S_1, which in facts corresponds to no erosion being performed at all, does not remove all tracers but keeps d at low values. By increasing the size of the structuring element to S_5 and S_9, e gets higher without deleting too much of the image yet. Beyond that for S_{13} and S_{21}, e remains in the same range but d increases. Overall, this is because larger S widen the areas detected as tracers more than smaller S when applying the erosion. This results in smaller S deleting less of I_{P} than larger ones but also being less likely to catch discrepancies between the position or shape of a tracer in I_{T} and in I_{P}. The images I_{P} and I_{T} used in these tests match one another with a precision of ± 1 pixel. This explains the better results obtained for S_5 and S_9 as these two elements extend the areas detected as tracers in B_{T} over that ± 1 pixel range for the final mask M.

This procedure confirms the trends mentioned in section 2.2 on the influence of the choice of th_{T} and S. These parameters need to be chosen carefully and tuned according to the images and the system used.

3.3 Particle matching test procedure

The second procedure is designed to test errors resulting specifically from an inadequate choice of the parameters th_{T} and S. A flowchart of this procedure can be found in figure 8. The objective here is to ensure that tracked particles can faithfully be recovered after the method has been applied, while still removing the tracers. To separate this test from errors coming from discrepancies between I_{P} and I_{T}, it is performed on images with a perfect superposition between the two cameras. To achieve this, an image where only particles are visible I_{P0} is taken and combined with a tracer image I_{T} into a synthetic image I_{C}. I_{C} is made by taking the maximal intensity between I_{P0} and I_{T} for each pixel: $I_{\mathrm{C}}(x, y) = \max(I_{\mathrm{P0}}(x, y), I_{\mathrm{T}}(x, y))$. By doing so, I_{C} has both particles and tracers, tracers perfectly match between I_{T} and I_{C}, and I_{P0} gives access to what I_{C} looks like without tracers. The goal is then to recreate I_{P0} by applying the tracer removal method to I_{C} and see if tracking results are the same when PTV is performed on I_{P0} and on I_{C} after removing the artificially added tracers. The tracer removal method is used on I_{C} which results in a masked image I_{M}, and PTV is then performed on I_{P0} and I_{M}. This gives access to the positions $\boldsymbol{r}_{\mathrm{P0}}$ and $\boldsymbol{r}_{\mathrm{M}}$ of particles successfully tracked in these images (i.e. particles for which a

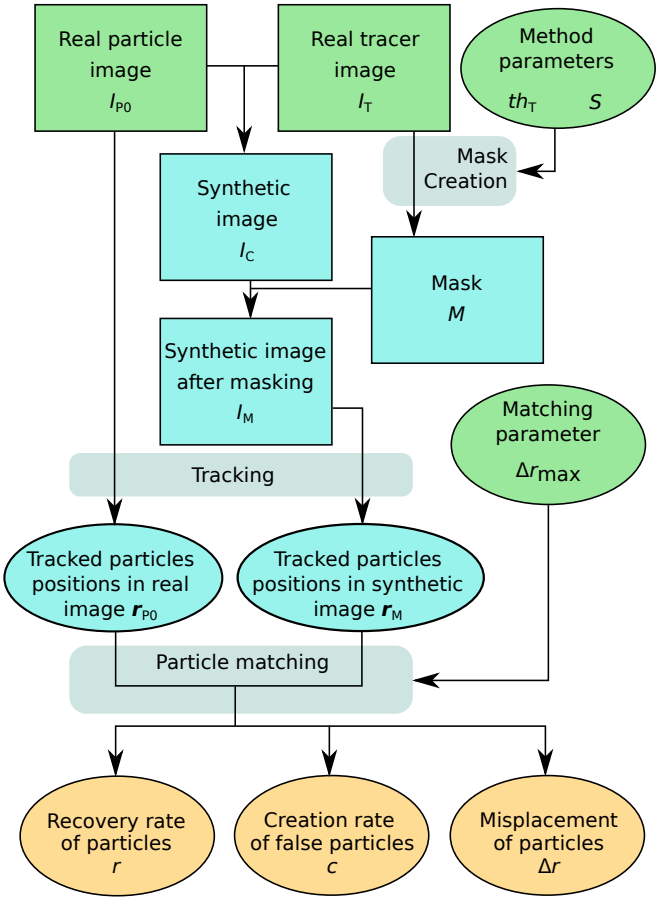

Fig. 8: Flowchart of the testing procedure on inadequate parameter choice.

track has been found, providing both particle position and velocity). A particle matching is then performed, by comparing the particle positions $\boldsymbol{r}_{\mathrm{P0}}$ and $\boldsymbol{r}_{\mathrm{M}}$, pairing particles in I_{P0} and I_{C} with a maximal distance between them of $\Delta r_{\max}$. Overall, the inputs of this testing procedure for a given pair of images I_{P0} and I_{T} are the method parameters th_{T} and S, and the matching parameter $\Delta r_{\max}$. After the particle matching is done, particles can be divided into three categories: particles only found in I_{P0}, particles only found in I_{M}, and particles that have been successfully matched between I_{P0} and I_{M}. The number of particles in each of these categories are denoted as N_{P0}, N_{M} and N_{b}, respectively. The rate of particle recovery r is then computed as: $r = N_{\mathrm{b}}/(N_{\mathrm{b}} + N_{\mathrm{P0}})$. r then varies between zero and one, with zero meaning that all initially tracked particles in I_{P0} were lost while going through the test, and one meaning that all of them where recovered. In the same manner, the tracers left in I_{M} appear as newly created particles, and correspond to the number N_{M}. Accordingly, the creation of false particles is computed by the creation rate c, given by: $c = N_{\mathrm{M}}/(N_{\mathrm{b}} + N_{\mathrm{P0}})$. Additionally, the particle matching gives the misplacement Δr for each particle detected in both I_{P0} and I_{M}, that is to say $\Delta r = ||\boldsymbol{r}_{\mathrm{M}} - \boldsymbol{r}_{\mathrm{P0}}||$.

An overview of the input parameters used in this procedure is presented in table 2. Although tests have been performed for all the structuring elements S presented in figure 3, the best results where systematically obtained with S_1, which is equivalent to not applying any erosion when making the mask. This is in line with the fact that, in this testing procedure, the images have a perfect superimposition, and the areas of the mask that will remove the tracers do not need to be extended to cover any discrepancies between the particle image and the tracer image. All data presented in this section hereafter is obtained using S_1 as the structuring element.

As $\Delta r_{\max}$ fixes the maximum misplacement error that can be measured in these tests, its value may influence the results obtained by the procedure. To avoid the introduction of biases, the mean recovery and creation rates $\langle r \rangle$ and $\langle c \rangle$ (averaged over all test cases for a given th_{T}) are plotted against $\Delta r_{\max}$ in figure 9. For $\Delta r_{\max}$ between 1 and 2 pixel, $\langle r \rangle$ and $\langle c \rangle$ saturate on plateaus whose values depend mainly on the chosen threshold th_{T}. This fixes an upper limit to the misplacement of particles by the method to 2 pixels, as increasing $\Delta r_{\max}$ beyond this value does not change the results. This limit can be high depending on the resolution of the system, but will be discussed further at a later point in this section. To further study r and c, $\Delta r_{\max} = 2$ pixels will be used in the following analysis.

For this procedure, a good parameter choice should result in high r and low c. Here, again, th_{T} is shown to be crucial. Scatter plots of r against c distinguished by th_{T} are represented in figure 10. Over these plots, as th_{T} increases, r increases overall to values getting closer to one. The values of c start spread over a 0 to 0.1 range for $th_{\mathrm{T}} = 10$. That range first decreases as th_{T} increases, reaching a minimal spread for $th_{\mathrm{T}} = 35$. For th_{T} values above that, the range of c values increases again. This confirms yet again that picking too low or too high of a value for th_{T} leads to poorer performance for the method, as low values generate masks that cover a larger area than necessary and high values fail to remove some tracers. Over the tests presented here, $th_{\mathrm{T}} = 35$ seems to achieves the best results.

By design of the test method, for each set of given inputs, $\Delta r \leq \Delta r_{\max}$. To obtain a finer measure of the misplacement error of the method, the distribution of Δr has to be studied. The misplacements Δr of all detected particles have been compiled in histograms such as the one presented in figure 11. All histograms obtained are heavily skewed toward low values for Δr, typically less than 0.1 pixel. To have a better estimation of the misplacement error, the median and 90^{th} percentile of the distribution of Δr have been computed for every test case. Figure 12 shows these quantities averaged for a given th_{T} and $\Delta r_{\max}$. Both the median and 90^{th} percentile of Δr have a minimal value reached for $th_{\mathrm{T}} = 35$ in the tested cases, confirming the previous result that this is the best value for th_{T} over the tests made in this procedure. In this case, half of the particles are on average misplaced by less than 0.05 pixel by the method, and 90% by no more than 0.21 pixel. These results are also stable for $\Delta r_{\max} > 2$ pixel, while values lower than that lead to slightly lower values of the median and 90^{th} percentile.

4 Method results

4.1 Recommendations

The starting step to use the method is to acquire the images. First, the tracer images should be suitable to perform PIV. This means having a sufficient tracer seeding in regard to the image resolution and the PIV interrogation windows, typically 3 to 5 tracer per interrogation window. However, as the method removes the part of the image that corresponds to tracers, it is recommended to aim at the lowest possible density in tracers that still allows PIV to be performed. This will of course be dependent on the acquisition system and on the PIV algorithm used. Secondly, the particle images should also enable PTV to be performed. Overall, this

Table 2: Overview of the parameters tested in the particle matching test procedure. For an illustration of the structuring elements' shapes, see figure 3. The images I_T and I_{P0} come from various experiments using tungsten carbide particles of diameter comprised between 63 µm and 75 µm and ceramic particles with diameters between 180 µm and 200 µm.

Parameter	**Values, range or number**	**Unit**
th_T	{10; 20; 35; 50; 70}	greyscale intensity
Δr_{max}	0.2 to 5	pixel
Structuring elements' shapes	S_1, S_5, S_9, S_{13}, S_{21}	-
Number of I_T	6	-
Number of I_{P0}	75	-
Tracer diameter	2 to 3	pixel
Particle diameter	4 to 7	pixel

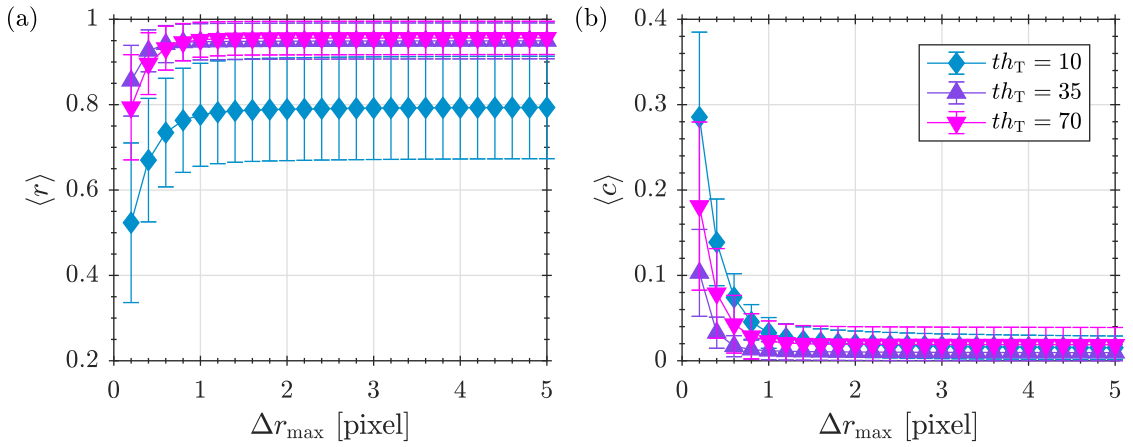

Fig. 9: Averages of r and c, as functions of Δr_{max}, coloured and separated by th_T. Only some values of th_T are presented here to show the general trends. The error bars are of one standard deviation above and below the mean value. Both $\langle r \rangle$ and $\langle c \rangle$ stabilise at plateau values reached generally between 1 to 2 pixels for Δr_{max}. These plateau values are mainly influenced by th_T.

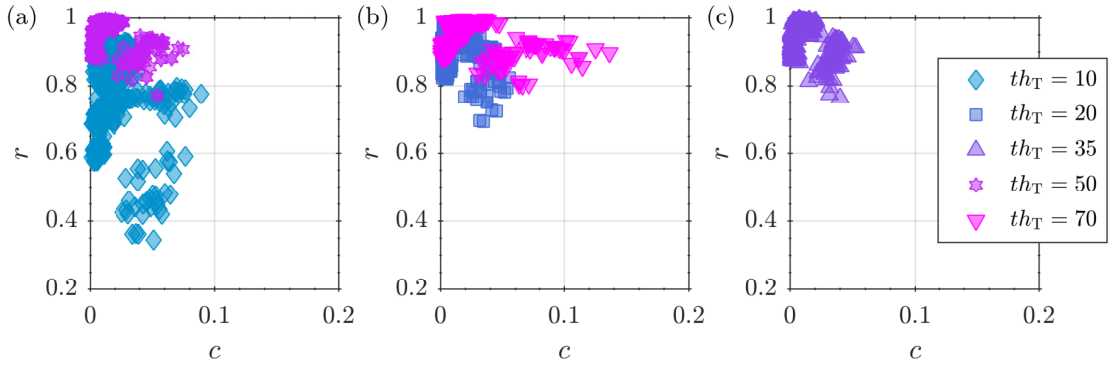

Fig. 10: Scatter plots of r against c for $\Delta r_{max} = 2$ pixel, distinguished by values of th_T. These are spread in three separate plots for clarity, to avoid overlapping too many points. The threshold that reaches high r and low c most consistently is $th_T = 35$.

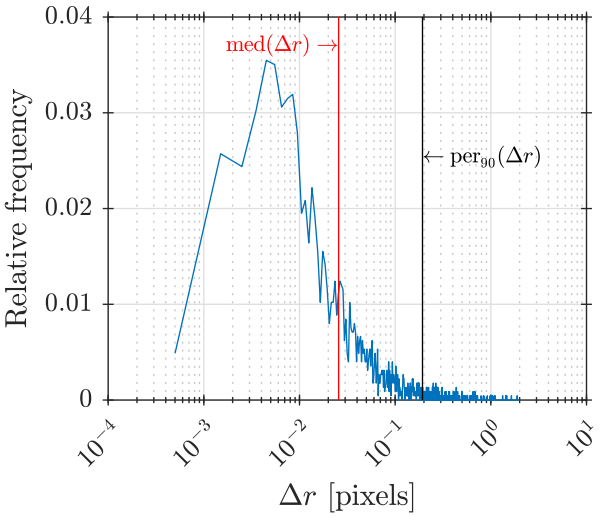

Fig. 11: Typical example of an histogram of Δr. The counts are normalised by the total number of samples (i.e., the number of particles successfully matched N_b) to obtain a relative frequency. This histogram comes from a test case with $th_\mathrm{T} = 35$, S_1 and $\Delta r_\mathrm{max} = 2$ pixels. The median and 90$^\mathrm{th}$ percentile of the distribution are marked by vertical lines.

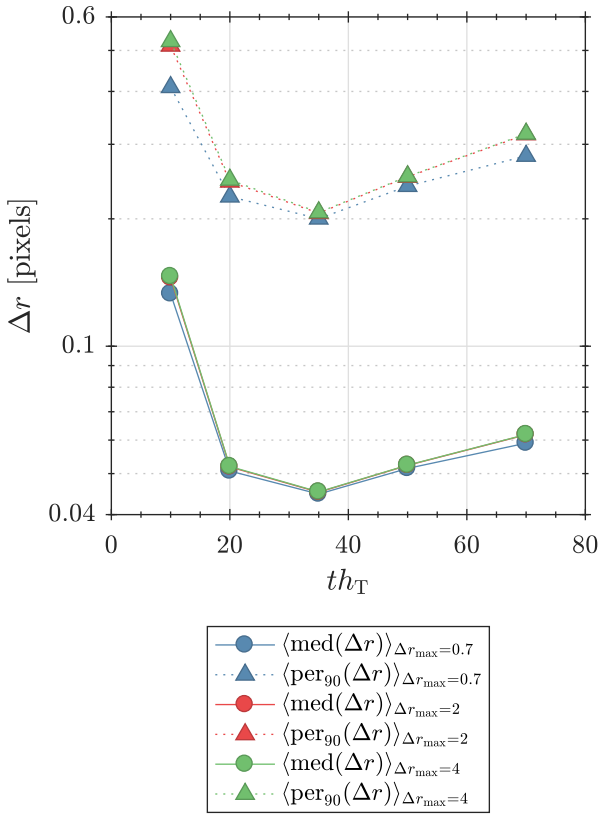

Fig. 12: Mean of the median and 90$^\mathrm{th}$ percentile of Δr over the tested cases against th_T, and separated by Δr_max. Three Δr_max have been chosen here to showcase the trends observed. The results for $\Delta r_\mathrm{max} = 2$ (in red) and $\Delta r_\mathrm{max} = 4$ (in green) are almost superimposed.

also translates to having a good resolution of the particles on the images to accurately find particle positions. Once again this will depend on the systems and algorithms used. For the acquisition system presented in section 3.1, having an apparent diameter of 5 pixels was enough to detect particle centers with sub-pixel precision. Finally, and perhaps most importantly, both image sources must be synchronised and calibrated in a way that allows them to be superimposed. The superposition should be as accurate as possible, to allow for a smaller structuring element S to be used which reduces the risk of erroneously deleting particles with the tracer mask (see section 3.2).

To use the method itself, the choice of th_T is the most important parameter to decide on, as evidenced by the tests of sections 3.2 and 3.3. th_T should be chosen so that it is above the background noise of I_T, to avoid the removal of portions of the image where no tracers are present. Other than that, we recommend to set th_T as low as possible to ensure all tracers are removed. Typically, for the images obtained from the experimental set-up described in section 3.1, $th_\mathrm{T} = 10$, when paired with S_9 results in almost all tracers being eliminated from I_P while still being able to track at the very least 80% of inertial particles.

The choice of the structuring element S is then also important. This will depend on how well I_P and I_T can be superimposed. In the case of a perfect superposition, (i.e., all tracers in both images perfectly overlap) no erosion (S_1) is required for the method to work correctly. Otherwise, a measure of how much disparity remains between I_P and I_T is needed to choose the structuring element. A simple approach is to perform a cross-correlation on sub-areas of images I_P and I_T when only tracers are visible. This is in fact similar to how the correction from the self-calibration method is computed (Wieneke, 2005), and akin to how PIV is performed in general. The resulting disparity map gives the remaining local misplacement between I_P and I_T. Then the larger the disparities are, the larger S will have to be. For example, for differences of ± 1 pixels, S_9 would be a good choice, as this element will cover all disparities in that range.

Finally, we would like to point that the structuring elements tested here where chosen to have no preferential orientation. This is because the present discrepancies between I_P and I_T did not show any preferred axis. However, depending on the experimental

set-up, anisotropic distortions can occur and remain consistent through time. Examples of such distortions include curved windows between the cameras and the laser sheet (e.g. cylindrical tanks) or astigmatism which can be induced by some optical filters. When such time-consistent distortions occur, S can also be deformed and stretched along the direction of these distortions.

4.2 Example results

This section showcases some results obtained with the tracer removal method. Those results come from an experiment where ceramic particles with diameters between 160 nm and 180 nm are settling in water. The fluid is initially quiescent and seeded with tracers coated in rhodamine. The experiment is performed in the experimental set-up described in section 3.1. The recording starts as soon as the seeding system is turned on ($t = 0$ s).

Figure 13 shows the evolution of the vertical velocity v_z of the detected particles over time. Histograms of v_z have been computed for each timestep and compiled into a colour plot. Additionally, the mode of the histogram is shown as a solid line. Negative values of v_z denote a downward motion of the particles. In the first instants, the particles have not reached the field of view of the cameras so any detected particles are false positives from tracers, which explains the histograms' modes lingering around $v_z \approx 0$. At $t = 12$ s particles start passing in the camera field of view and can be detected. The first cloud of particles falls with a settling speed of $v_z \approx -0.32$ m/s. In their wake, subsequent particles are accelerated to velocities of $v_z \approx -0.42$ m/s ($t \approx 40$ s). Finally, the particles reach a stationary behaviour ($t > 90$ s) while falling with a velocity of $v_z \approx -0.34$ m/s.

Figure 14 shows two examples of instantaneous particle velocities and fluid vertical velocity fields from the same experiment. They were taken at $t = 20$ s for figure 14a and $t = 60$ s for figure 14b to have similar average particle velocities. Figure 14a shows the particles settling in a column with a downward fluid flow. The same can be said for figure 14b, however the number of particles is smaller and the downward fluid flow is more intense and localised in the column of settling particles. The evolution of the fluid velocity flow suggest the development of large scale flows in the experimental set-up.

The tracer removal method could then give access to data from both phases simultaneously and showcase the importance of having access to both velocity fields to better study dispersed two-phase flow systems. Statistics on the evolution of other relevant quantities such as the local slip velocity (i.e., the difference between the particle velocity and the fluid velocity at the position of the particle) will be investigated in future studies.

5 Conclusion

A method to distinguish particles from tracers in the study of dispersed two-phase flow has been developed. This method relies on the use of both optical filtering paired with adequately dyed tracers (rhodamin coated tracers in this case) and post-processing operations to segregate inertial particles from tracers. This tracer removal method can function properly even when particles and tracers are undistinguishable in size or intensity through usual visualisation techniques. The method was tested to ensure its proper operation, and to assess its response to various input parameters. From these tests, suitable parameters for the method were found. Although these parameters are specific to the experimental set-up on which the method is used, general rules on how to properly choose them have been provided. This method works on a variety of particle material and size, opening the possibility to access large ranges of the parameter space experimentally.

Conflict of interest

The authors declare that they have no conflict of interest.

Appendix: Exemplary implementation

This section outlines an example implementation of the tracer removal method in MATLAB R2016b. The particle image I_P and the tracer image I_T are stored in the variables `I_P` and `I_T`, respectively, as $(N_1 \times N_2)$-matrices of type `uint16`. The position of the tracers in I_T are detected by a threshold value th_T of, for example, 35.

```
>> th_T = 35;
>> B_T = I_T < th_T;
```

The variable `B_T` holds the binarised image B_T. For the erosion of B_T, the structure element S_5 is chosen.

```
>> S_5 = [0 1 0; 1 1 1; 0 1 0];
>> M = imerode(B_T, S_5);
```

The variable `M` is a $(N_1 \times N_2)$-matrix of type `logical` containing the tracer mask M. To calculate the masked particle image I_M, the mask is applied to I_P.

```
>> I_M = I_P .* cast(M, 'like', I_P);
```

The variable `I_M` is a $(N_1 \times N_2)$-matrix of type `uint16` and contains the image I_M with only particles remaining. It can now be further evaluated, for example, by applying a PTV algorithm.

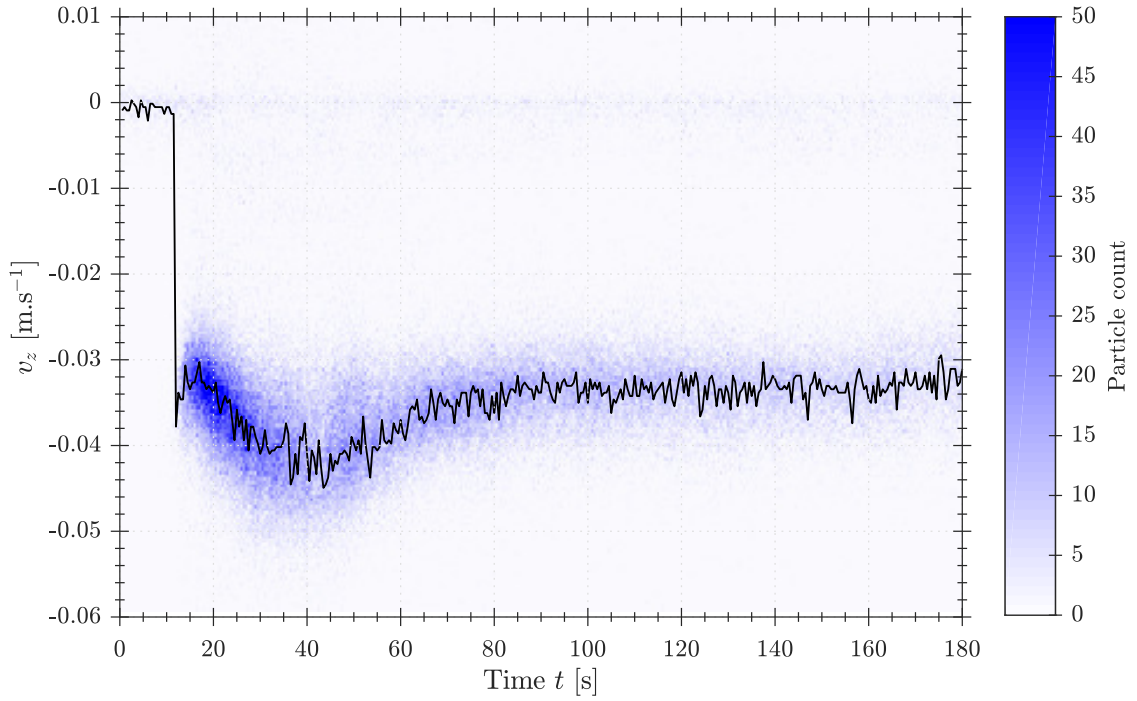

Fig. 13: Temporal histogram the vertical velocity v_z for ceramic particles of diameters between 160 nm and 180 nm settling in quiescent water. The black line corresponds to the mode of the histogram at each instant in time. The vertical axis z of the experiment is oriented upward, so falling particles have negative velocities.

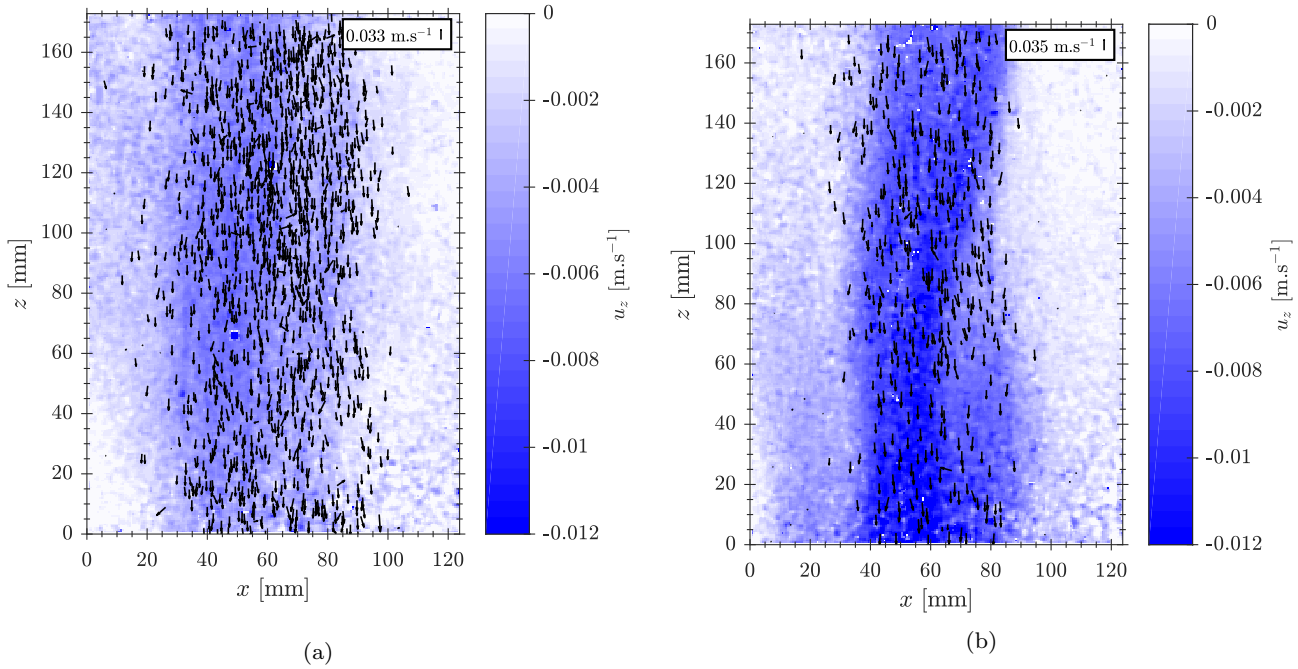

Fig. 14: Instantaneous particle velocities (arrows) and fluid vertical velocity fields u_z (color-plot) at (a) $t = 20$ s and (b) $t = 60$ s, of the same experiment shown in figure 13. Arrows of the average velocity magnitude of the particles are in the top-left corners of each plot for scale.

References

Aliseda A, Cartellier A, Hainaux F, Lasheras JC (2002) Effect of preferential concentration on the settling velocity of heavy particles in homogeneous isotropic turbulence. Journal of Fluid Mechanics 468:77–105

Brown GL, Roshko A (1974) On density effects and large structure in turbulent mixing layers. Journal of Fluid Mechanics 64:775–816

Chen R, Fan LS (1992) Particle image velocimetry for characterizing the flow structure in three-dimensional gas-liquid-solid fluidized beds. Chemical Engineering Science 47(13-14):3615–3622

Eaton JK (2009) Two-way coupled turbulence simulations of gas-particle flows using point-particle tracking. International Journal of Multiphase Flow 35(9):792–800

Elghobashi S, Truesdell G (1993) On the two-way interaction between homogeneous turbulence and dispersed solid particles. I: Turbulence modification. Physics of Fluids A: Fluid Dynamics 5:1790

Elhimer M, Praud O, Marchal M, Cazin S, Bazile R (2017) Simultaneous PIV/PTV velocimetry technique in a turbulent particle-laden flow. Journal of Visualization 20(2):289–304

Falkovich G, Fouxon A, Stepanov MG (2002) Acceleration of rain initiation by cloud turbulence. Nature 419:151–154

Gatignol R (1983) The Faxen formulae for a rigid particle in an unsteady non-uniform Stokes flow. Journal de Mécanique Théorique et Appliquée 2:143–160

Gustavsson K, Mehlig B (2011) Ergodic and non-ergodic clustering of inertial particles. Europhysics Letters 96(6):60012

Haralick RM, Sternberg SR, Zhuang X (1987) Image Analysis Using Mathematical Morphology. IEEE Transactions on Pattern Analysis and Machine Intelligence PAMI-9(4):532–550

Hassan Y, Blanchat T, Seeley Jr C, Canaan R (1992) Simultaneous velocity measurements of both components of a two-phase flow using particle image velocimetry. International Journal of Multiphase Flow 18(3):371–395

Homann H, Bec J (2010) Finite-size effects in the dynamics of neutrally buoyant particles in turbulent flow. Journal of Fluid Mechanics 651:81–91, 0909.5628

Huck P, Bateson C, Volk R, Cartellier A, Bourgoin M, Aliseda A (2018) The role of collective effects on settling velocity enhancement for inertial particles in turbulence. Journal of Fluid Mechanics 846:1059–1075

Khalitov D, Longmire E (2002) Simultaneous two-phase piv by two-parameter phase discrimination. Experiments in Fluids 32(2):252–268

Kiger K, Pan C (2000) PIV technique for the simultaneous measurement of dilute two-phase flows. Journal of Fluids Engineering 122(4):811–818

Lucci F, Ferrante A, Elghobashi S (2010) Modulation of isotropic turbulence by particles of Taylor length-scale size. Journal of Fluid Mechanics 650:5

Maxey M, Corrsin S (1980) Stokes spheres falling under gravity in cellular flow-fields. APS Bulletin 25:paper EA6

Maxey MR, Riley JJ (1983) Equation of motion for a small rigid sphere in a nonuniform flow. Physics of Fluids 26:883–889

Monchaux R, Dejoan A (2017) Settling velocity and preferential concentration of heavy particles under two-way coupling effects in homogeneous turbulence. Physical Review Fluids 2(10):104302

Mora DO, Aliseda A, Cartellier A, Obligado M (2018) Pitfalls measuring 1d inertial particle clustering. In: iTi Conference on Turbulence, Springer, pp 221–226

Muste M, Fujita I, Kruger A (1998) Experimental comparison of two laser-based velocimeters for flows with alluvial sand. Experiments in Fluids 24(4):273–284

Ouellette NT, OMalley P, Gollub JP (2008) Transport of finite-sized particles in chaotic flow. Physical Review Letters 101(17):174504

Petersen AJ, Baker L, Coletti F (2019) Experimental study of inertial particles clustering and settling in homogeneous turbulence. Journal of Fluid Mechanics 864:925–970

Poelma C, Westerweel J, Ooms G (2007) Particle fluid interactions in grid-generated turbulence. Journal of Fluid Mechanics 589:315–351

Towers D, Towers C, Buckberry C, Reeves M (1999) A colour PIV system employing fluorescent particles for two-phase flow measurements. Measurement Science and Technology 10(9):824

Wieneke B (2005) Stereo-PIV using self-calibration on particle images. Experiments in Fluids 39(2):267–280